Nanotechnology

PAPER

Desalination behavior analysis of interior-modified carbon nanotubes doped membrane by dielectric spectrum and molecular simulation

To cite this article: Qing Li *et al* 2020 *Nanotechnology* **31** 315705

View the article online for updates and enhancements.

IOP ebooks™

Bringing together innovative digital publishing with leading authors from the global scientific community.

Start exploring the collection–download the first chapter of every title for free.

This content was downloaded from IP address 210.31.76.58 on 19/05/2020 at 12:25

IOP Publishing Nanotechnology

Nanotechnology **31** (2020) 315705 (17pp) https://doi.org/10.1088/1361-6528/ab8988

Desalination behavior analysis of interior-modified carbon nanotubes doped membrane by dielectric spectrum and molecular simulation

Qing Li[1], Kongshuang Zhao[1], Qingzhi Liu[2] and Jianhua Wang[2]

[1] College of Chemistry, Beijing Normal University, Beijing 100875, People's Republic of China
[2] College of Chemistry and Pharmaceutical Sciences, QingDao Agriculture University, QingDao 266109, People's Republic of China

E-mail: zhaoks@bnu.edu.cn and liuqz2001@163.com

Received 8 November 2019, revised 20 February 2020
Accepted for publication 15 April 2020
Published 13 May 2020

Abstract

Carbon nanotube (CNT)-doped polyamide (PA) membranes have attracted much attention in reverse osmosis (RO) membranes due to their significant advantages of water flux and desalination. In this study, we synthesized multi-walled carbon nanotube (MWNT)/PA RO membrane by 12-oxodidodecanoic acid methyl ester group interior-modified MWNTs (MWNT-$C_{14}H_{25}O_4$). Then, their mechanism of desalination behavior was successfully analyzed by combining dielectric relaxation spectrum (DRS) and molecular dynamics (MD) simulation. DRS analysis mainly focuses on two aspects: (1) the water volume fraction, average pore size and dielectric parameters of MWNT-$C_{14}H_{25}O_4$/PA and PA membranes were obtained by model analysis of DRS data. These data of MWNT-$C_{14}H_{25}O_4$/PA membrane are higher than PA membrane, which indicates that the water flux of the MWNT-$C_{14}H_{25}O_4$/PA membrane was higher than that of the PA membrane. (2) Further analysis shows that the MWNT-$C_{14}H_{25}O_4$/PA membranes have high average charge density, ion solvation barrier and reflection coefficient, which indicates that the added interior-modified MWNT can improve the salt rejection of PA membranes. In the microscopic aspect, the desalination behavior of the MWNT-$C_{14}H_{25}O_4$/PA and PA membrane was analyzed from the aspects of free volume distribution, the dynamic diffusion process of water and ions. The results show that the microscopic data of dynamic simulation well support the conclusion of the DRS method. This study provides a convenient methodology to characterize the properties of the membrane from the aspect of membrane structure.

Keywords: MWNT-$C_{14}H_{25}O_4$/PA membrane, dielectric relaxation spectrum, molecular dynamics, interior-modified

(Some figures may appear in colour only in the online journal)

1. Introduction

Reverse osmosis (RO) desalination, known as 'water purification technology in the 21st century', has become one of the most reliable methods to desalinate seawater and brackish water [1]. However, the performance of most widely used commercialization polyamide (PA) membranes falls within a well-known trade-off problem between flow and salt rejection, that is, high water flux and high salt rejection are difficult to achieve simultaneously [2, 3]. Therefore, nowadays, many studies have been focusing on modifying PA membranes to achieve high water flux and salt rejection simultaneously [4, 5]. Nanotechnology provides a new route to address the issues. For example, nano-sized zeolites could increase water

 © 2020 IOP Publishing Ltd Printed in the UK

flux without reducing salt rejection, which is due to the change of microstructure and macroscopic properties of membranes by adding nanoparticles [6, 7].

Among the choices of nanomaterials, carbon nanotubes (CNTs) show promising results as building blocks for nano-engineered membranes to use in many fields due to their remarkable properties. For example, Mantzalis and Drikakis show that MWNTs have a promising future on the CO_2 adsorption [8–10], transport [11] and separation [12] by molecular dynamics (MD) simulation. Some simulations [13, 14] and experiments [15] also demonstrated that water can transport narrow CNTs freely. Furthermore, the water flow rate through CNTs driven by pressure was three to five orders of magnitude higher than what was predicted by theoretical value theoretical calculations [15, 16]. In view of this, studies of CNTs embedded in PA composite membranes have been reported by many researchers [17–19] such as Zhang *et al* [20] and Zhao *et al* [21]. Compared to the PA membrane, the water flux of these MWNT/PA membranes was significantly increased, but the salt rejection increased a little or even decreased slightly. Corry [22] and Chan *et al* [23] found that the salt rejection of CNTs could increase with adding modified groups at the entrance by MD simulation and experiments. For example, four NH_3^+ or eight COO^- groups modified at the (8, 8) CNT (with a diameter of 1.1 nm) entrance could increase the salt rejection from 59% to 100% [22]. However, it was difficult to achieve high desalination for larger diameter CNT modification with functional groups only on entry [24].

Recent studies have shown that CNT hydrophobic pores are similar to aquaporin-4, which is an excellent water channel that can reject all ions [25, 26]. Inspired by the structure of narrow pore channels with amino acid residues inside the aquaporin-4 channel protein, we used MD simulation to simulate CNT/electrolyte systems. The results showed that the improving salt rejection rate of CNTs modified by functional groups (–COOH, $–CONH_2$, $–NH_2$ or long-chain functional groups) in the interior and/or at entrances simultaneously was higher than the rate gained only by entrance modification [27, 28]. Based on these simulation studies, MWNT/PA composite membrane compositions of MWNT (4.9 nm diameter) modified by 1-ethyl 12-methyl dodecanedioate ($C_{14}H_{25}O_4$) at the tip and interior were prepared for desalination (see section 2.1 for details). The results showed that the water flux and salt rejection of the MWNT-$C_{14}H_{25}O_4$/PA membranes, compared with the PA membranes, were increased by 21.7% and 5.07% [29], respectively.

The desalination behavior of RO membrane is normally determined by their structure and morphology. Therefore, it is crucial to get the parameters that show the effective structural features for understanding the details of membrane transport mechanism. The common methods of membrane structure detection, such as scanning electron microscopy (SEM), x-ray photoelectron spectroscopy and atomic force microscopy usually give some information on the surface morphology of dry membranes. While the characteristics under working conditions are more closely related to membrane performance and the separation mechanism, such as being soaked in solutions. Dielectric relaxation spectrum (DRS) or electrochemical impedance spectroscopy was widely used to acquire the information of polarized behavior of heterogeneous systems, especially those composed of polymer membranes and electrolytes (membranes in working conditions) [30–32]. Many studies on special phenomena in different membrane/solution systems have been reported, such as concentration polarization [33], pore dielectric properties [34], fouling [35] and ion selectivity [36]. In our previous studies [21, 31, 32], the permittivity and conductivity of the membrane in working conditions were obtained with a certain model. Moreover, some parameters such as pore radius, ionic binding energy and reflection coefficient could be obtained to analyze the membrane separation mechanism. At microscopic level, computer simulations offered unique opportunities to link macroscopic properties and microscopic physical phenomena. Recently, a great deal of research has studied the structure and ion transport in polymeric membrane and CNT hybrid membranes by using MD simulation [37–40].

In this work, we developed a new generation of PA RO membranes doped with 12-oxodidodecanoic acid methyl ester group interior-modified multi-walled carbon nanotubes (MWCNTs). In order to theoretically analyze the desalination behavior of the MWNT-$C_{14}H_{25}O_4$/PA membranes and to design the RO membrane targeted in the next stage, the systems composed of MWNT-$C_{14}H_{25}O_4$/PA membranes, PA membranes and different concentrations of NaCl solution were studied by DRS based on the theory of interface polarization. In addition, the ion transport mechanism of the MWNT-$C_{14}H_{25}O_4$/PA membranes was further analyzed from the microstructure using all-atom MD methods.

2. Material and methods

2.1. Materials and sample preparation

2.1.1. Materials. MWNTs (average diameter of 4.9 nm) were purchased from Beijing Deke Island Gold Technology Co., Ltd, while M-Phenylenediamine (MPD) and 1,3,5-trimesoyl chloride (TMC) were bought from Tianjin Beilian Fine Chemicals Development Co., Ltd and Shanghai Maclean Biochemical Technology Co., Ltd, respectively. Dodecanedioic acid was bought from Shanghai McLean Biochemical Technology Co., Ltd. PSF membranes were obtained from Shenzhen Jiaquan Membrane Filter Equipment Co. Ltd. All other reagents were used as received, such as dimethylformamide (DMF), ethyl alcohol, concentrated sulfuric acid and lithium aluminum hydride ($LiAlH_4$).

2.1.2. Synthesis of methyl 12-chloro-12-oxododecanoate. Dodecanedioic acid, methanol solution and concentrated sulfuric acid were refluxed at 70 °C for 24 h to obtain dimethyl dodecanedioate. Dimethyl dodecanedioate and potassium hydroxide (KOH) were dissolved in methanol solution and then kept stirred for 4 h continuously at room temperature. Then, the product was acidified with hydrochloric acid to obtain dodecanedioicacid-1-methylester.

The dodecanedioicacid-1-methylester was dissolved in anhydrous toluene at 5 °C with an ice bath, then two drops of DMF and 5 ml oxalyl chloride were added in turn. Then, reduced pressure distillation was used to obtain the expected CNT-modified functional group methyl 12-chloro-12-oxododecanoate.

2.1.3. MWNT functionalization. MWNTs and mixed acid (H_2SO_4:HNO_3 = 3:1) were stirred under reflux at 60 °C for 4 h to obtain acidified MWCNTs (MWNT-COOH). Then, MWNT-COOH was reduced to MWNT-CH_2OH by the reducing agent $LiAlH_4$. MWNT-CH_2OH, DMF and pyridine solution reacted with functional group 12-chloro-12-oxodidodecanoate for 2 h in ice water to obtain long-chain-modified CNTs MWNT-$C_{14}H_{25}O_4$.

2.2. Membrane fabrication

2.2.1. PA membranes. PA membranes were obtained by interfacial polymerization (IP) reaction with 2.0% m-phenylenediamine (MPD) (with 0.1% sodium dodecyl sulfate (SDBS)) (aqueous phase) and 0.2% trimesoyl chloride (TMC) solutions (oil phase) on the surface of fixed PSF membranes.

2.2.2. Functionalized MWNT nanocomposite membranes. In the IP step, 0.05% MWNT-$C_{13}H_{25}O_4$ was added to the aqueous phase. Other steps were the same as the process of PA membrane fabrication. The detailed process of the synthesis of functional groups and preparation and characterization of membranes were shown in the literature [24].

2.3. Characterization

2.3.1. MWNTs and membrane characterization. The morphology of pristine MWNTs and functionalized MWNTs was observed by transmission electron microscope (TEM) (JEM 2100F). The graft ratio of functionalized MWNTs was characterized by thermogravimetric analysis (TGA) (HCT-1, 12-036). The performance of the membranes was characterized by a contact angle goniometer (DSA100, Germany) and SEM (JEOL 7500F, Japan).

2.3.2. Membrane permeation tests. The filtration performances of both the PA and MWNT-$C_{14}H_{25}O_4$/PA membranes were evaluated by using a cross-flow filter with an effective membrane area of 20.41 cm^2. The membrane filtration pressure was maintained at 1.0 MPa and the feed solution concentration was 2000 mg l^{-1} NaCl solution (brackish water concentration) according to the literature [17]. The conductivity of the feed solution was 3.0 mS cm^{-1}, and the temperature was controlled at 298 K. The membrane permeation flux was measured by collecting permeate water for 1 min and weighing it after compression at 1.0 MPa for 2 h. The water flux and salt rejection of the membranes were calculated according to equations (1) and (2), respectively.

$$J = \frac{\Delta V}{A \times \Delta t}, \tag{1}$$

where ΔV and Δt are difference values of water volume and time interval (h) between two measurements, respectively, where A is the effective surface area (cm^2) of the membrane.

$$R = (1 - \frac{C_p}{C_f}) \times 100\%, \tag{2}$$

where R is salt rejection, C_p and C_f are the concentration of the permeate solution and feed solution, respectively. The salt concentration can be measured by a conductivity meter during this process.

2.4. Dielectric relaxation spectroscopy

DRS measurement was performed using an HP 4294A Precision Impedance Analyzer (Angilent, Japan) with a measurement frequency of 40 Hz107 MHz, an AC voltage of 500 mV at room temperature (21°). The measuring unit consists of a pair of platinum plate electrodes with an area (S) of 3.14 cm2 and a cell constant (S/L) of 2.415 cm (L is the distance between the two electrodes). When measured, the PA or MWNT-$C_{14}H_{25}O_4$/PA RO membranes were respectively sandwiched in a measuring solution filled with a low-concentration solution of NaCl solution (0.005 ~ 10 mmol l^{-1}), as shown in figure 1(a). Therefore, this system could be considered to be composed of two phases, which are the membrane phase with capacitances C_m and solution phase (the solution on both sides of the membrane is the same) with capacitances C_w. Figures 1(b) and (c) show the equivalent circuit for describing the dielectric spectrum of the system according to Maxwell's theory. In order to reduce the error, all the dielectric measurements were repeated three times. The results show that this method has good reproducibility.

The experimental errors caused by stray capacitance (C_r), battery constant (C_l) and residual inductance (L_r) are corrected by the Schwan method [41]. These were obtained by three criteria substances (pure water, ethanol and air) and varying concentrations of KCl solution. Their values were 0.934 pF, 0.214 pF and 24.1 μH, respectively. The modified capacitance data C_s and conductance G_s are converted to capacitance and conductivity by equation (3) and (4), where ε_0 represents vacuum permittivity.

$$\varepsilon = (C - C_r)/C_l, \tag{3}$$

$$\kappa = G\varepsilon_0/C_l. \tag{4}$$

2.5. Dynamic simulation models

A schematic illustration demonstrating the structure of the MWNT-$C_{14}H_{25}O_4$/PA membrane is presented in figure 2. As shown in figure 2, the MWNT-$C_{14}H_{25}O_4$/PA composite membranes contain three layers, which are the active layer (MWNT-$C_{14}H_{25}O_4$/PA layer), PSF layer and non-woven fabric layer. The PA membranes also contain these three layers, while the active layer is a PA layer. Because the desalination rate of the RO membrane depends on the performance of the active layer, we only focused on the desalination behavior (ion

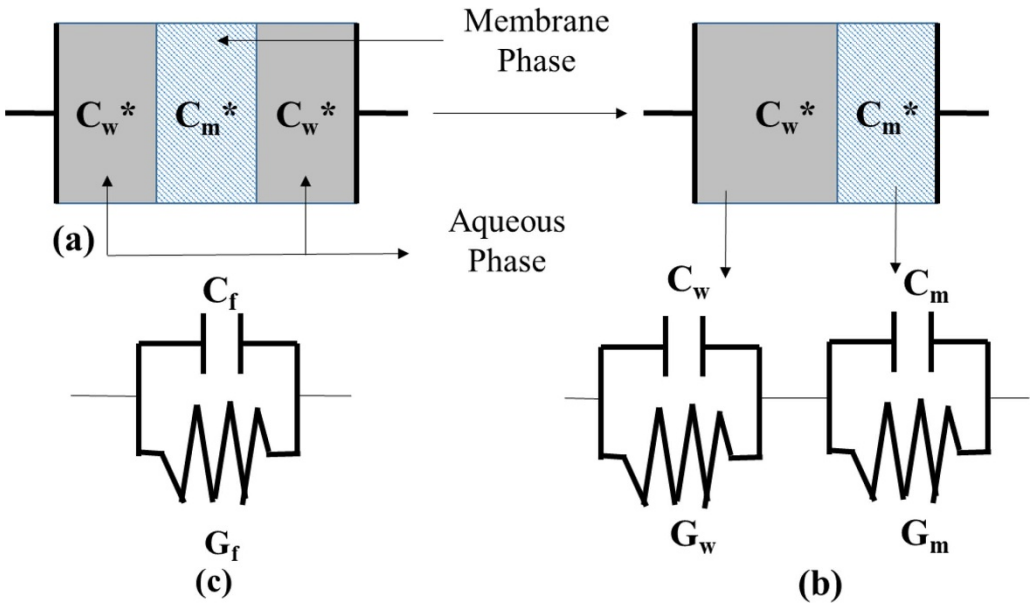

Figure 1. Dielectric model of the system of membrane/solution. (a) Measurement system; (b) equivalent circuit model of (a); (c) equivalent capacitance $C(f)$ and conductance $G(f)$ of the whole cell system.

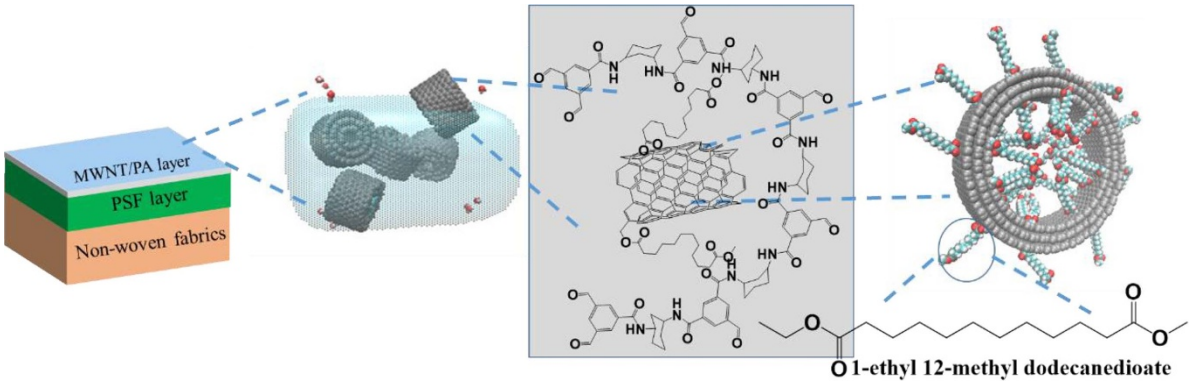

Figure 2. Structure of MWNT-$C_{14}H_{25}O_4$/PA membranes.

selectivity and water flux performance) of the active layer by MD methods in this work. In this paper, all the membrane structure construction and MD simulations were carried out by Materials Studio software 6.0 package (Accelrys Inc).

To simulate the active layer (PA layer) of PA membrane, a PA chain was folded into the simulation box with a degree of polymerization, ten repeated units, as shown in figure 3(a). The structural monomer and repeating unit of the PA chain model are shown in figures 4(a)–(c). For the active layer (MWNT-$C_{14}H_{25}O_4$/PA nanocomposite layer) of the MWNT-$C_{14}H_{25}O_4$/PA membrane, the simulation model contains, in addition, a PA chain with a degree of polymerization, 10 repeated units, and a 1-ethyl 12-methyl dodecanedioate modified MWNT (figure 3(b)).

In the initial stage, a 10 000 structure optimization was carried out by a forcite module to eliminate bad contact (extremely twisted, stretched or compressively deformed bonds and angles). Next, was the annealing process, by which the system was heated from 300 to 600 K at 50 K intervals and then cooled. Afterwards, a 200 ps NPT constant atomic number, pressure and temperature simulation was performed to obtain the equilibrium molecular density and a 200 ps NVT constant atomic number, volume and temperature simulation was adopted to obtain the equilibrium molecular structure of the membranes. Finally, a 1000 ps NVT simulation was calculated for the subsequent analysis. In the simulation process, energy minimization was performed by the smart minimizer method. Andrea *et al* [42] and Berendsen *et al* [43] methods were using to control the temperature and pressure, respectively. The force field parameters were taken from COMPASS27 [44]. The van der Waals force was described by the Ewald method and the Coulomb force was described by the atom-based method. The non-band cut-off distance was 1.45 nm and the time steps were set to 0.5 fs.

3. Results and discussion

3.1. Characterization of MWNTs and membranes

As shown in figure 5, four curves of thermal weight loss in the fabrication process of MWNT modification with long-chain

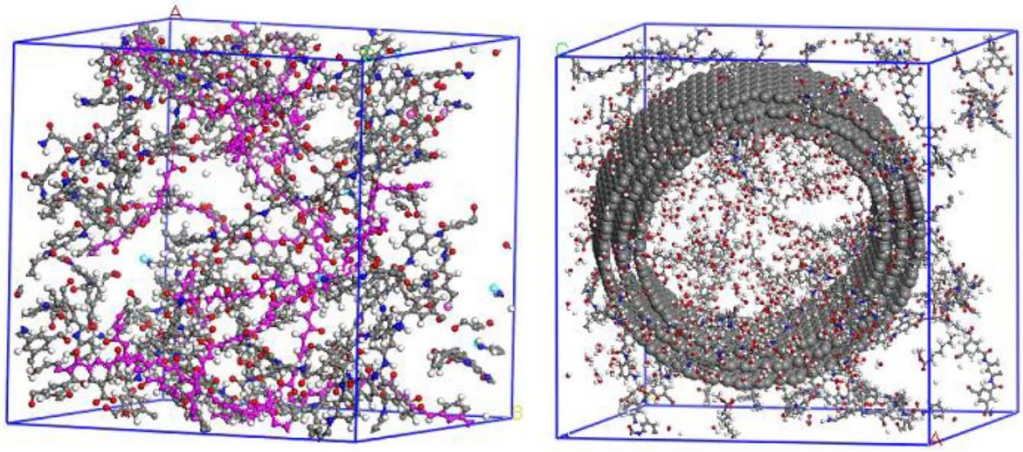

Figure 3. Model of (a) PA membrane and (b) MWNT-$C_{14}H_{25}O_4$/PA membrane.

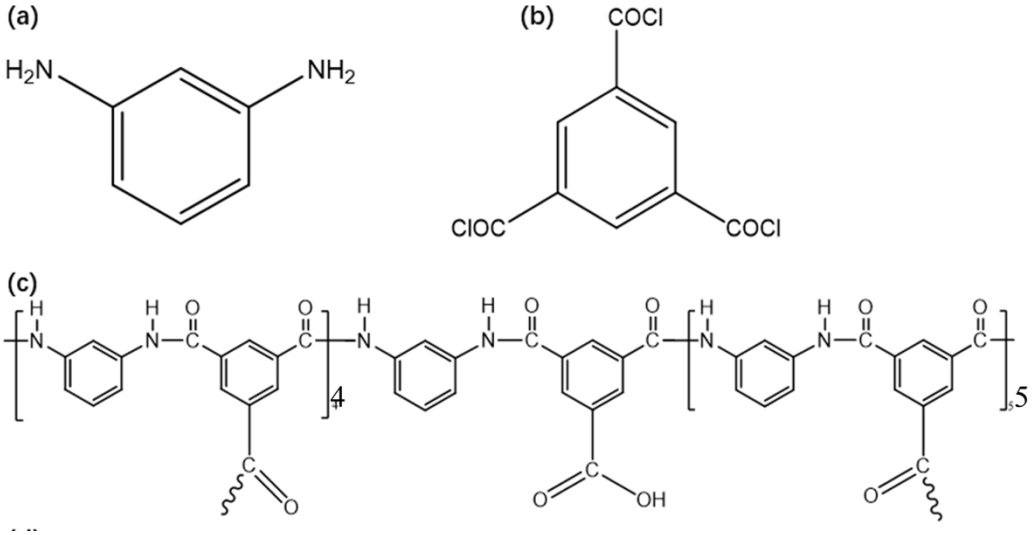

Figure 4. (a) m-Phenylenediamine (MPD), (b) 1,3,5-phthalic acid molecular (TMC) and (c) a repeat unit of PA molecular chain.

functional group 1-ethyl 12-methyl dodecanedioate were different, which indicated that the desired functional groups were connected to the MWNTs successfully. The inner diameter of MWNT modification with 1-ethyl 12-methyl dodecanedioate functional groups was 2.8 nm, which was smaller than that of unfunctionalized MWNT. This meant that the 1-ethyl 12-methyl dodecanedioate groups were successfully grafted into the interior of the MWNT, as shown in figure 6. Table 1 shows the results of membrane permeation and contact angle tests. As shown in table 1, compared with the PA membrane, the water flux and salt rejection of the MWNT-$C_{14}H_{25}O_4$/PA membrane were increased by 21.7% and 5.07%, respectively, and the contact angle of MWNT-$C_{14}H_{25}O_4$/PA was decreased by 36.84%.

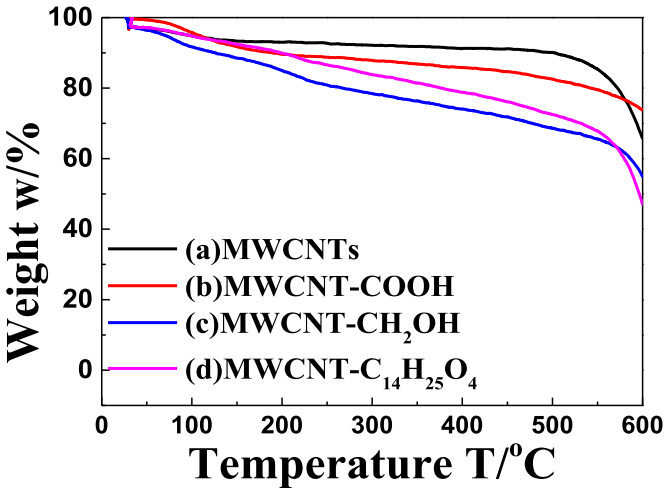

Figure 5. TGA of the process of MWNT grafting of long-chain functional groups.

3.2. Dielectric behavior of PA and MWNT-$C_{14}H_{25}O_4$/PA membrane

Figure 7 shows the concentration-dependent 3D representations of dielectric loss spectra ($\varepsilon'' - f$) of the system of PA, MWNT-$C_{14}H_{25}O_4$/PA membrane and NaCl solution. The illustration in figure 7 is the 2D diagrams cut by concentration. Figure 7 shows two significant dielectric relaxations near 10^2

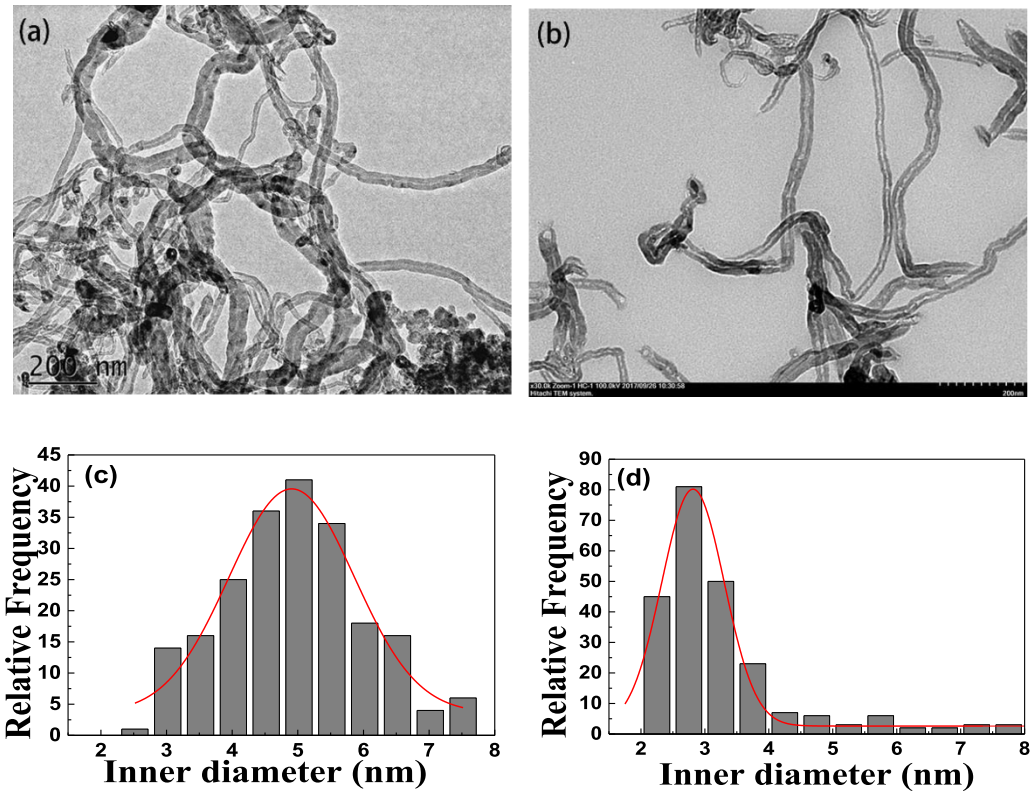

Figure 6. TEM micrograph of (a) original MWNTs, (b) MWNT-$C_{14}H_{25}O_4$ distribution of inner diameter, (c) original MWNTs and (d) MWNT-$C_{14}H_{25}O_4$.

Table 1. Water flux, salt rejection and contact angle of PA and MWNT-$C_{14}H_{25}O_4$/PA membranes.

Membrane	PA	MWNT-$C_{14}H_{25}O_4$/PA	Rate of increment (%)
Water flux (L (m^2 h)$^{-1}$)	10.92±0.09	13.29±0.11	21.70%
Salt rejection (%)	86.01±0.72	90.37±0.82	5.07%
Contact angle (°)	41.61±0.36	26.28±0.23	−36.84%

and 10^6 Hz for the two membranes, which are low- and high-frequency relaxation. The two relaxations are characterized by high-, middle- and low-frequency permittivity and conductivity, and low- and high-characteristic relaxation frequency. The representation symbols are $-\varepsilon_h$, ε_{mid}, ε_l, κ_h, κ_{mid}, κ_l, f_l and f_h, respectively. As shown in our previous research [32], the eight dielectric parameters were obtained by Cole–Cole complex planes. The frequency dielectric parameters for PA and MWNT-$C_{14}H_{25}O_4$/PA membrane/NaCl solution at various concentrations are shown in tables 2 and 3, respectively.

3.2.1. Low-frequency relaxation. The relaxation time (τ) is the most effective criterion to determine different types of dielectric relaxation mechanism. Thus, for convenient understanding, the well-known Einstein equation was introduced to analyze the relaxation mechanism.

$$\tau = \langle x \rangle^2 / 2D, \tag{5}$$

where ⟨x⟩ is the average displacement and D is the average diffusion coefficient of ions. When an electric field was imposed on the system, the counter ions near membrane pores could transport from one side of the membrane to the other side at relatively low frequencies. However, with the increasing of the electric field frequency, the counter ions near membrane pores could not keep up with the change of applied electric field. So, counter ions would oscillate in a very small range rather than transport through the membrane pore, which usually led to a lower frequency relaxation. According to dielectric theory of membrane systems [45, 46] and our previous research [47] on membrane/electrolyte systems, we infer that the low-frequency relaxation is caused by 'counter-ion polarization'. As shown in tables 2 and 3, the parameter $\Delta\varepsilon_l$ of low-frequency relaxation is increasing linearly on the concentration, which agrees with our previous research [47]. The increasing $\Delta\varepsilon_l$ can be attributed to the increase of concentration gradient of electrolyte solution near the membrane pore.

3.2.2. High-frequency relaxation. Compared to low-frequency counter-ion polarization interfacial polarization is attributed to the induced electric field generated by the charge ions gathered at the interface of the membrane that

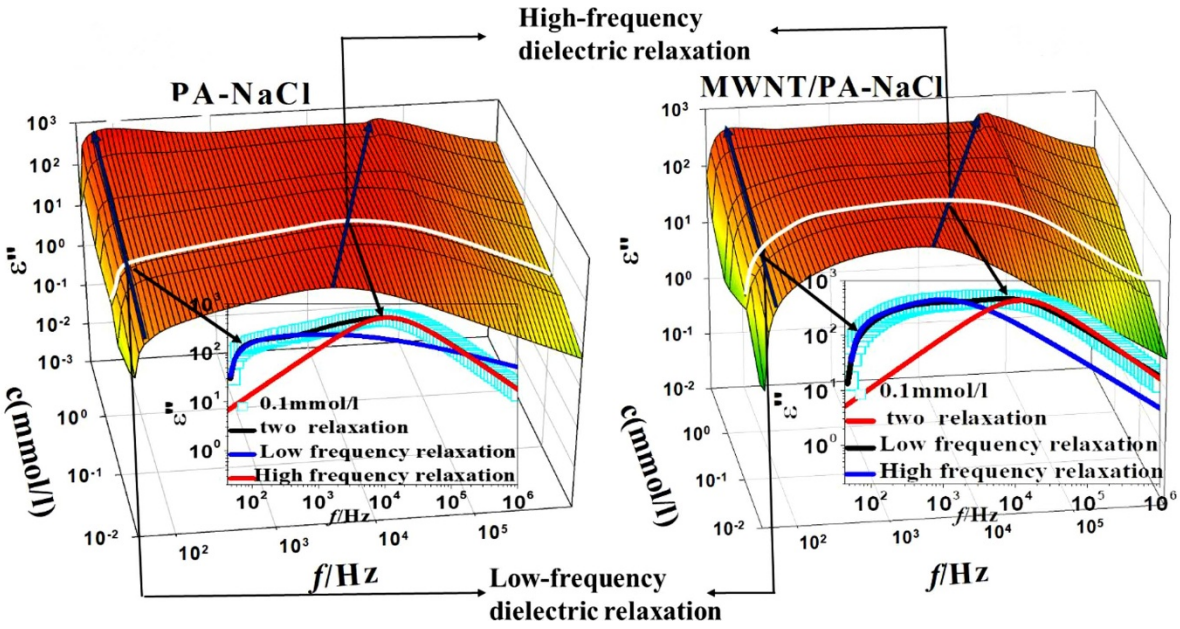

Figure 7. 3D characterization of the concentration dependence of dielectric loss spectra for the (a) PA-NaCl system and (b) MWNT-$C_{14}H_{25}O_4$/PA-NaCl system. Insets show the 2D diagrams cut at the concentration.

could not keep up with the frequency change of applied AC electric field. As shown in tables 2 and 3, the parameter high-frequency relaxation $\Delta\varepsilon_h$ was almost unchanged following the increase of solution concentration, whereas f_h and $\Delta\kappa_h$ linearly related to the concentration. This showed remarkable characteristics of interfacial polarization [48], and so the high-frequency relaxation was considered to be caused by interfacial polarization mechanism.

The high-frequency relaxation phase parameters C_m, G_m, $C_w$and G_w could be obtained by dielectric parameters ε_h, ε_{mid}, $\kappa_h$and κ_{mid} by equations (3) and (4). The specific solution process of dielectric parameters and phase parameters can be found in [32]. Dielectric parameters ε_m, κ_m, $\varepsilon_w$and κ_w can be converted by phase parameters with the membrane area (S), the distance (L) between the electrodes and the membrane thickness (t) parameters, as listed in tables 2 and 3.

3.3. Estimation of membrane's characteristic parameters

3.3.1. Water flux. The dielectric constant of membrane phase in the solution was greater than that in dry state, which was due to the larger dielectric constant electrolyte solution entering the membrane. Thus, the dielectric constant of wet membrane can also be expressed by the membrane's water volume fraction f_w, which can be calculated by equation (6) [49]. Calculation results are shown in figure 8.

$$\varepsilon_m = \varepsilon_w f_w + (1 - f_w)\,\varepsilon_m', \tag{6}$$

where $\varepsilon_m'$and ε_w represent the dielectric constant of dried polymer membranes and solution, respectively. As shown in figure 8, the concentration dependency of f_w and ε_m have the same trend. The f_w decreased following the increasing of concentration and finally tends to unchanged, as shown in figure 8(a). The reason for this phenomenon could be interpreted as follows: the membranes consisted of charged polymer materials, and there is an empty space in the polymer matrix, i.e. pore channels. When counter ions in solution entered into the pore channel, electrostatic repulsion force between polymer backbones would be shielded, gradually forming a relatively dense state, thus reducing the pore size of the polymer. With the increase of counter-ion concentration, the fixed charge was completely shielded and the increase of electrolyte concentration no longer affects the aggregation state of the polymer backbones. Therefore, f_w decreased under low concentration and remained unchanged in the range of 0.5–10 mol m^{-3} NaCl concentration.

As shown in figure 8, the water volume fraction f_w of MWNT-$C_{14}H_{25}O_4$/PA was larger than the PA membrane. The phenomena could be attributed to the empty space (pore size) of the polymer matrix of the MWNT-$C_{14}H_{25}O_4$/PA membrane being larger than the PA membrane due to the presence of large-diameter MWNT. The aggregation extent of polymer chains in the MWNT-$C_{14}H_{25}O_4$/PA membrane by counter ions was smaller than the PA membrane. Moreover, an additional water channel was provided by the MWNT and the rigid natural pores of MWNT were not affected by the anti-ion shielding charge. Thus, this caused more water molecules to enter the MWNT-$C_{14}H_{25}O_4$/PA membrane. Otherwise, as shown in table 1, the contact angle of the MWNT-$C_{14}H_{25}O_4$/PA membranes was smaller than the PA membrane, which indicated the hydrophilicity of MWNT-$C_{14}H_{25}O_4$/PA membranes was higher than PA membrane. The increased hydrophilicity of MWNT-$C_{14}H_{25}O_4$/PA membranes makes it easier for water molecules to approach the surface of the membrane. Thus, the number of water molecules entering the membrane increases. Therefore, these two reasons indicated that water flux of the MWNT-$C_{14}H_{25}O_4$/PA membrane was larger than that of the PA membrane, which is in agreement with the result of

Table 2. Dielectric parameters of PA membrane in various concentrations of NaCl solution.

c (mmol l^{-1})	$\Delta\varepsilon_l$	$\Delta\varepsilon_h$	f_h (Hz)	$\Delta\kappa_h$ (μs m^{-1})	ε_m	ε_w	κ_m (S/m*10^{-7})	κ_w (S/m*10^{-3})
0.01	190.55 ± 1.61	1163.21 ± 11.11	3568.40 ± 32.33	23.08 ± 0.17	12.4 ± 0.1	79.1 ± 0.2	3.18 ± 0.03	0.29 ± 0.01
0.05	538.73 ± 2.32	1160.29 ± 10.28	13 120.68 ± 30.71	84.67 ± 0.34	11.0 ± 0.2	78.9 ± 0.3	5.82 ± 0.03	1.02 ± 0.01
0.1	655.48 ± 2.60	1153.00 ± 9.63	14 487.35 ± 28.56	92.89 ± 0.35	10.8 ± 0.1	79.1 ± 0.3	5.85 ± 0.04	1.12 ± 0.01
0.5	935.52 ± 5.11	1149.13 ± 9.87	20 935.60 ± 34.53	133.99 ± 1.12	10.3 ± 0.2	80.5 ± 0.2	5.83 ± 0.03	1.58 ± 0.01
1.0	1293.18 ± 10.12	1134.99 ± 11.11	28 266.65 ± 23.21	178.69 ± 1.31	10.2 ± 0.2	80.2 ± 0.3	7.74 ± 0.05	2.11 ± 0.02
5.0	2193.82 ± 13.78	1132.85 ± 10.38	41 577.56 ± 39.12	262.00 ± 2.18	10.2 ± 0.1	80.6 ± 0.2	1.14 ± 0.11	3.10 ± 0.02
10.0	2734.57 ± 12.56	1128.77 ± 9.72	54 888.29 ± 41.14	344.52 ± 2.87	10.2 ± 0.1	80.4 ± 0.2	1.49 ± 0.10	4.08 ± 0.03

Table 3. Dielectric parameters of MWNT-$C_{14}H_{25}O_4$/PA membrane in various concentrations of NaCl solution.

c (mmol l^{-1})	$\Delta\varepsilon_l$	$\Delta\varepsilon_h$	f_h (Hz)	$\Delta\kappa_h$ (μs m^{-1})	ε_m	ε_w	κ_m (S/m$^*10^{-7}$)	κ_w (S/m$^*10^{-3}$)
0.01	436.13 ± 2.31	1163.21 ± 12.23	3503.49 ± 33.18	23.08 ± 0.19	13.8 ± 0.1	78.7 ± 0.2	6.88 ± 0.04	0.27 ± 0.01
0.05	593.86 ± 2.73	1160.29 ± 13.35	5557.82 ± 46.35	84.67 ± 0.43	11.4 ± 0.1	78.4 ± 0.2	5.81 ± 0.06	0.41 ± 0.01
0.1	663.1 ± 4.18	1153.00 ± 11.81	7892.52 ± 67.73	92.89 ± 0.51	11.2 ± 0.1	79.1 ± 0.3	4.18 ± 0.03	0.62 ± 0.01
0.5	842.89 ± 7.65	1149.13 ± 10.38	17 266.87 ± 89.28	133.99 ± 0.67	10.7 ± 0.2	80.3 ± 0.2	5.76 ± 0.03	1.34 ± 0.01
1.0	1032.34 ± 9.81	1134.99 ± 11.29	24 472.32 ± 99.11	178.69 ± 0.88	10.7 ± 0.1	80.5 ± 0.3	8.12 ± 0.08	1.90 ± 0.01
5.0	1298.51 ± 10.11	1132.85 ± 13.75	28 361.23 ± 106.35	262.00 ± 1.12	10.7 ± 0.2	80.0 ± 0.3	9.33 ± 0.08	2.19 ± 0.02
10.0	1426.82 ± 11.27	1128.77 ± 14.13	32 002.01 ± 233.23	344.52 ± 1.21	10.6 ± 0.1	80.9 ± 0.3	10.51 ± 0.11	2.46 ± 0.02

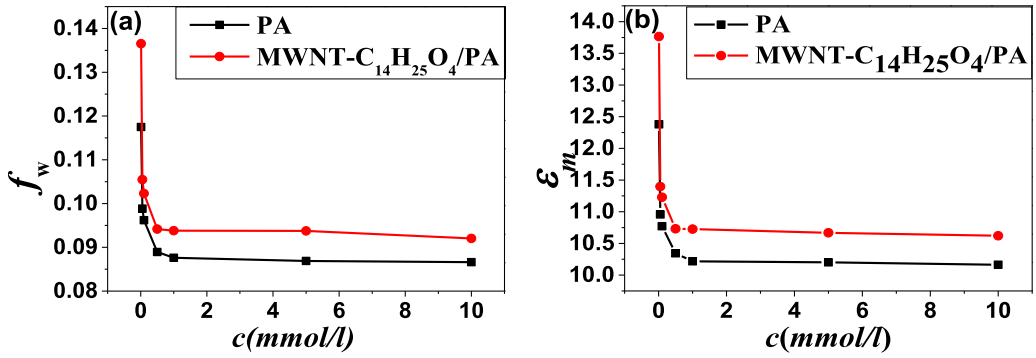

Figure 8. Plots of (a) the water volume fraction f_w and (b) permittivity of PA membrane (black line) and MWNT-$C_{14}H_{25}O_4$/PA membrane (red line) against NaCl concentrate.

the water flux test shown in table 1 (water flux of MWNT-$C_{14}H_{25}O_4$/PA membranes is increased by 21.7% compared to the PA membrane).

3.3.2. Pore structure of membrane. Using positron annihilation spectroscopy and MD simulation, Simazu *et al* [50] and Harder *et al* [51] demonstrated that RO membranes had pores, as shown in figure 9. A work on the MD simulation of CNT/PA RO membranes published by Araki *et al* [39] also showed that plain PA membrane and CNT/PA membranes all had pore distributions. Therefore, in this paper, we further illustrated the mechanism of water flux improvement from the pore structure of membrane.

As proved in section 3.1 and our previous paper [47], the low-frequency relaxation of the membrane/solution system was associated with membrane pores. According to our previous paper [47], we simplified the porous PA membrane to the dielectric model shown in figure 9(c). In this dielectric model, membrane pores (simplified to cylinder pores) filled with electrolyte solution (dispersed phase), are dispersed in the continuous phase (membrane active layer base material). In the MWNT-$C_{14}H_{25}O_4$/PA membrane, although MWNT provided additional pore distributions, only 0.05% MWNTs was added to the PA layer and dispersed in all directions. Moreover, the long-chain function modification in MWNT also cross-linked with polymer chain, which formed pores similar to that of polymer membrane. Therefore, all the pores in the MWNT-$C_{14}H_{25}O_4$/PA membrane (including PA chain pores and MWNT pores) were also simplified to cylinder pores in this paper.

In the cylinder pores, the low-frequency relaxation time corresponded to the duration for the counter ions transporting through the pores from one side of the pore to the other side under the applied electric field E, as shown in figure 9(d). In this case, a represents the counter ions that migrate in the cylinder pores (pore length) and b represents the pore radius.

Thus, structural parameters of the membrane pores could be obtained by fitting the low-frequency relaxation with equation (7), which was derived by Takashima [52] and corrected by introducing the distribution coefficient β and the polarization term from our previous work [47].

$$\varepsilon_m(f) = \frac{e^2\sigma_0 a^2}{bkT\varepsilon_0}\frac{9\pi p}{2(1+p)^2}\frac{1+\left(\frac{f}{f_0}\right)^{\beta}\cos\left(\frac{\pi}{2}\beta\right)}{1+2\left(\frac{f}{f_0}\right)^{\beta}\cos\left(\frac{\pi}{2}\beta\right)+\left(\frac{f}{f_0}\right)^{2\beta}} + A\omega^{-m} + \varepsilon_h, \tag{7}$$

where σ_0 is electric charge density, p represents volume fraction of particles in the system, e represents elementary charge, K represents Boltzmann constant, T represents absolute temperature, f_0 is characteristic relaxation frequency, ω is angular frequency and $A\omega^{-m}$ denotes electrode polarization where A and m are determined by experimental methods.

The average pore size b and pore length a (thickness of PA layer) of the two membranes were obtained by fitting equation (7). Figure 10 is a typical fitting diagram of PA membrane and NaCl solution system. It shows that the fitting curve (red line) coincided with measured data at low-frequency range. The average pore radius of the MWNT-$C_{14}H_{25}O_4$/PA membrane was 0.320 nm, which was 30.61% larger than that of the PA membrane (0.245 nm) shown in table 4. The results of the pore radius also confirmed the assumption of section 3.1. The thickness of the active layer of the two membranes was a constant value (0.20 μm, a value in equation (7)). These values of average pore radius and active layer thickness of PA membrane were near the experimental values reported [3, 53]. These results confirm that the model established in this section is conformable and reasonable for analyzing the low-frequency relaxation of the RO membrane. The pore dielectric parameter of the MWNT-$C_{14}H_{25}O_4$/PA membrane ε_p was 29.4, which was 50.0% larger than that of the PA membrane (19.6) by calculation from equation (8) [54] with membrane average pore size data obtained by equation (7). The improving pore dielectric parameter of the MWNT-$C_{14}H_{25}O_4$/PA membrane also showed that more water molecules entered into the pores of the MWNT-$C_{14}H_{25}O_4$/PA membrane.

$$\varepsilon_p = \varepsilon_w - 2(\varepsilon_w - \varepsilon_d)\left(\frac{d}{r_p}\right) + (\varepsilon_w - \varepsilon_d)\left(\frac{d}{r_p}\right)^2. \tag{8}$$

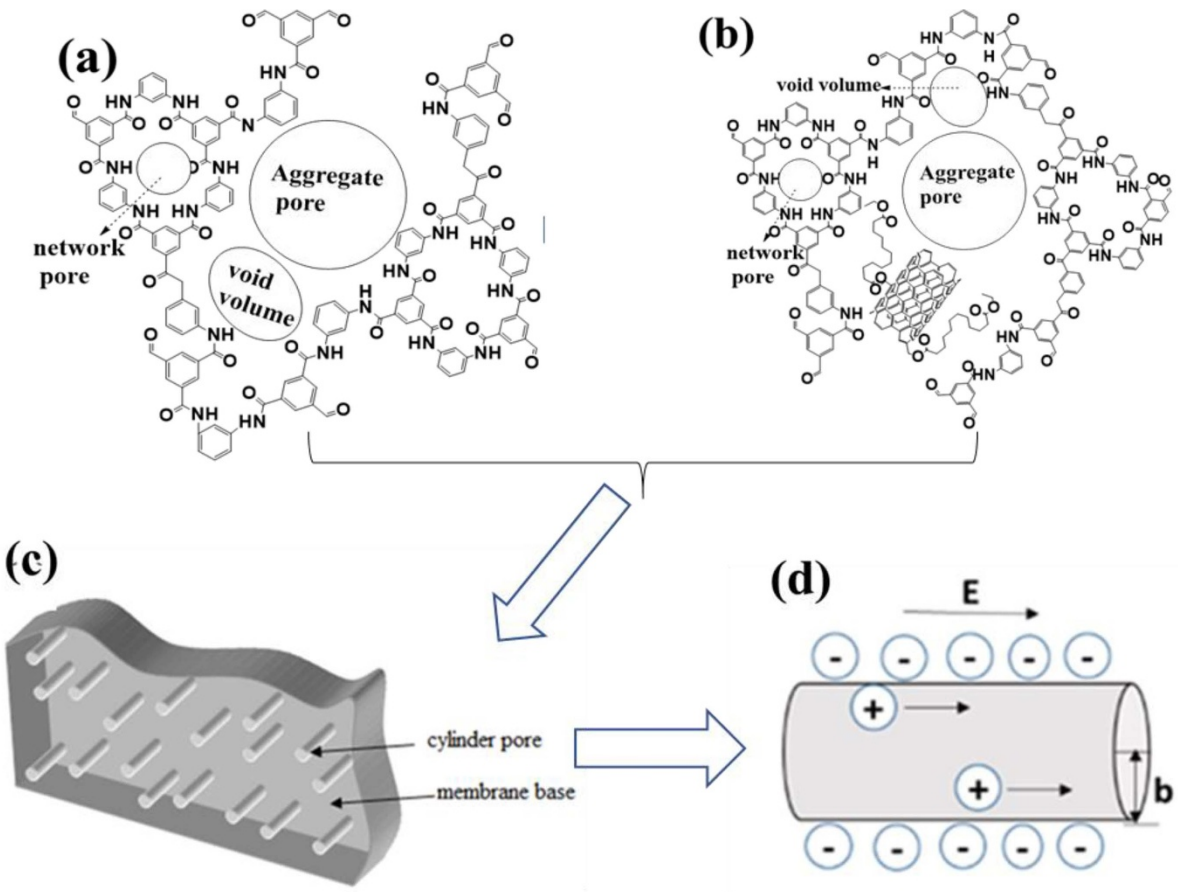

Figure 9. Pores of (a) PA membranes, (b) MWNT-C14H25O4/PA membranes, (c) dielectric model of two membrane active layers filled with cylindrical pores in electrolyte solution and (d) schematic diagram of the transport of counter ions in the pores, where *b* is the radius of the pores, *a* is the length of the pores and E is the applied electric field.

Table 4. Pore size of the PA and MWNT-$C_{14}H_{25}O_4$/PA membranes calculated by DRS and MD methods.

	Pore radius (nm)		
Membrane	DRS data	MD data	Experiment data [54]
PA	0.245 ± 0.002	0.241 ± 0.002	0.255
MWNT-$C_{14}H_{25}O_4$/PA	0.320 ± 0.003	0.318 ± 0.003	—
Rate of increment (%)	30.61%	31.95%	—

From our previous work, it is implied that the pore walls were composed of a layer of oriented water molecules in equation (8), where ε_d and d are the permittivity and thickness of this layer, respectively. ε_d is 6 and d is 0.28 nm, according to the literature [55].

Therefore, the improvement of pore size, pore dielectric parameter and water volume fraction f_w can be used to explain the increasing water flux of the MWNT-$C_{14}H_{25}O_4$/PA membrane from a mechanism perspective.

3.3.3. Volume charge density. It is generally believed that the separation mechanism of the RO process is related to the electrostatic distribution or electrostatic interaction between the charged membrane and the external solution. Therefore, Donnan equilibrium (or Donnan exclusion) and dielectric exclusion are often used to explain these problems [56]. According to the Donnan equilibrium, the ion selectivity of the membrane is mainly determined by the valence of the common ion, and to a lesser extent by the valence of the counter ion. Volume charge density (X_m) played an important role in the evaluation of the membranes' separation performance, where the ion could interact with the fixed charge in the membrane due to Donnan potential. According to the discussions in section 3.3.1, κ_m/κ_w decreased with increasing concentration and remains unchanged after the concentration reached 0.5 mmol l^{-1}. This was due to the influence of counter-ion charge shielding (the plots of κ_m/κ_w against c for the PA and MWNT-$C_{14}H_{25}O_4$ membranes and the fitting curve by equation (9) are shown in figure 11). Thus, according to the Donnan equilibrium principle and fixed charge model (TMS), the relation between X_m and bulk solution κ_m/κ_w was expressed by

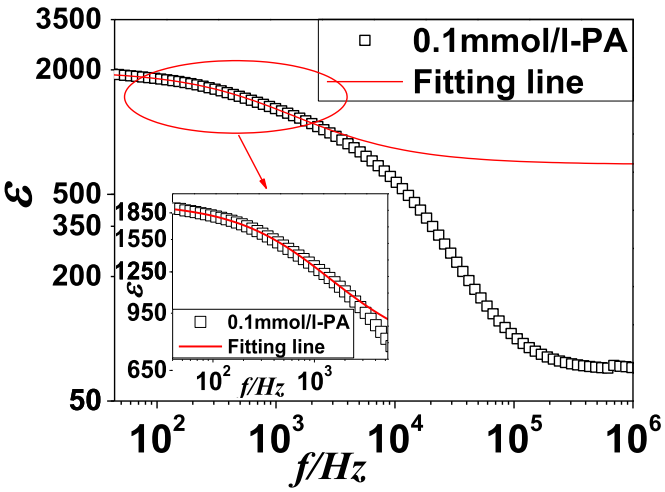

Figure 10. Dielectric constant dependence of frequency of system of PA membrane and 0.1 mmol l^{-1} NaCl solution. Curve is the fitting result by equation (7).

equation (9), as established in our previous paper [32].

$$\frac{\kappa_m}{\kappa_w} = \frac{U_+^m t_+^w}{U_+^w t_+^m}\left[\sqrt{\left(\frac{c_e}{2c}\right)^2 + 1} + \left(t_+^m - t_-^m\right)\frac{c_e}{2c}\right], \qquad (9)$$

where $U_m{}^+$, $U_m{}^-$, $U_w{}^+$and $U_w{}^+$ represent ion mobility while $t_m{}^+$, $t_m{}^-$, $t_w{}^+$and $t_w{}^+$ are defined as ion transport number. The values of X_m in the two membranes are all negatively charged by fitting expression (8). The volume charge density X_m of the MWNT/PA membrane and PA membrane were 0.386 and 0.237 mol m^{-3}, respectively. The overall negative charge of the MWNT-$C_{14}H_{25}O_4$/PA membrane was greater than that of the PA membrane, which was due to the ester group and carboxyl group with negative charge in the modified group of MWNT. Therefore, the higher volume charge density of the MWNT-$C_{14}H_{25}O_4$/PA membrane speculated that the attraction between electrostatic interactions of Na^+ ions and MWNT-$C_{14}H_{25}O_4$/PA membrane and repulsive force of Cl^- ions and MWNT-$C_{14}H_{25}O_4$/PA membrane were larger than that of the PA membrane, which was beneficial to the improvement of salt rejection of the MWNT-$C_{14}H_{25}O_4$/PA membrane.

3.3.4. Solvation energy barrier. The repulsion of ions by the charged membrane was caused by the electrostatic interaction between the ions in the solution and the polarized charge on the surface of the polymer membrane. On the other hand, because the polarized charges and ions in the solution have the same charge, the interaction brings additional repulsion effects. Moreover, the repellent effect will change as the dielectric constant of the solvent in the pores of the membrane changes. Thus, dielectric exclusion and energy barrier existed and strongly influenced ions for entering into membrane pores with low permittivity from solution with high permittivity, which would clearly influence salt rejection of the membranes. Based on the above principles, Hagmeyer and

Table 5. Ion solvation energy barrier of ions in different membranes obtained by equation (10).

ΔW_i ($*10^{-20}$ J)	Na^+	Cl^-
PA	2.39 ± 0.02	3.20 ± 0.03
MWNT-$C_{14}H_{25}O_4$/PA	2.57 ± 0.03	3.27 ± 0.03

Gimbel [57] and Bowen and Welfoot [58] proposed an empirical method to explain the change of the dielectric constant between the pores and the bulk solution: the equation indicates the change in the electrostatic free energy between ions. Considering the change of electrostatic free energy (or dielectric constant) between ions in bulk solution and membrane pore, based on the Born equation, the ionic solvation barrier expressions of sodium ion and chloride ion are proposed, in which only the dielectric constant of the membrane is taken into account (equation (10)) [31].

$$\Delta w_i = \frac{z_i^2 e^2}{8\pi\varepsilon_0 r_s}\left(\left(\frac{1}{\varepsilon_p} + \frac{0.393}{\frac{r_p}{r_s\varepsilon_m}}\left(1 - \frac{\varepsilon_m}{\varepsilon_p}\right)^2\right) - \frac{1}{\varepsilon_w}\right), \qquad (10)$$

where r_s is the Stokes radius of ions. Calculation results are shown in table 5. Results show that the solvation energy of Cl^- was greater than that of Na^+ in both membranes, which could be because it was easier for the counter-ion Na^+ to gain a preferential chance to enter the membrane pore (both membranes were negatively charged). Therefore, Na^+ met less barrier to enter the membrane's pore than Cl^- and had a smaller solvation barrier. The solvation energy of ions in the MWNT-$C_{14}H_{25}O_4$/PA membrane was larger than that of the PA membrane, which meant that ions were more difficult to transport through the MWNT-$C_{14}H_{25}O_4$/PA membrane. The increasing solvation energy of ions in the MWNT-$C_{14}H_{25}O_4$/PA membrane could be attributed to two different phenomena. The first of these arose from steric blockages of the pore, where more counter-ion Na^+ was strongly attracted to the ester and acyl amino functional group of MWNT-$C_{14}H_{25}O_4$, which was due to the MWNT-$C_{14}H_{25}O_4$/PA membrane having a larger volume charge density. The consequence of this was that the effective area of Cl^- was reduced. A more general reason for the increased ion solvation barrier of the MWNT-$C_{14}H_{25}O_4$/PA membrane was the introduction of significant direct interactions between the ions and the ester and acyl amino functional groups of the MWNT-$C_{14}H_{25}O_4$/PA membranes. Therefore, Na^+ and Cl^- met a higher solvation barrier in the MWNT-$C_{14}H_{25}O_4$/PA membrane. These agreed with the results of our salt rejection rate test shown in table 1 (compared to the PA membranes, the salt rejection rate of the MWNT-C14H25O4/PA membranes was increased by 5.07%).

3.4. MD simulation

The above results obtained by DRS exhibit superior performance for water flux and salt rejection of the MWNT-$C_{14}H_{25}O_4$/PA membranes from a macroscopic view. Theoretically, DRS data were related to the membrane's microstructure. Therefore, the credibility of these results may

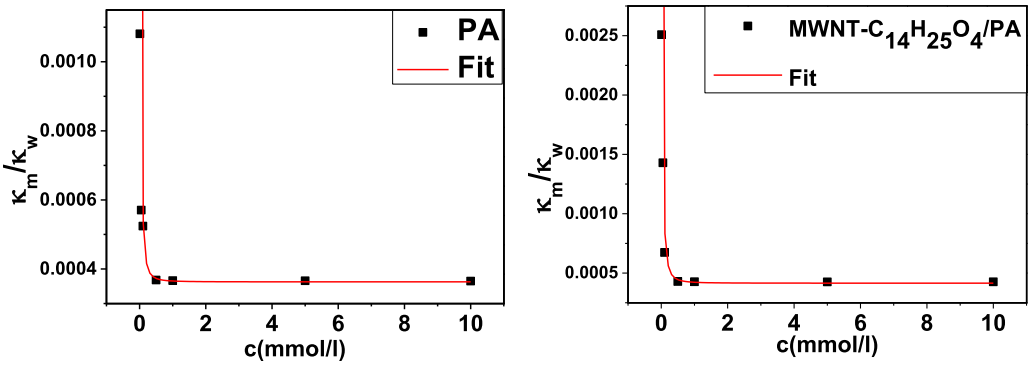

Figure 11. Plots of κ_m/κ_w against c for PA and MWNT-$C_{14}H_{25}O_4$ membranes and the fitting curve by equation (8).

be supported by theoretical calculation such as MD simulation, as described in the introduction.

3.4.1. Fractional free volume (FFV) and pore-size distributions. Free volume plays a crucial role to characterize the pore structure and diffusion process of polymeric membranes and can be determined accurately by MD simulation. In this paper, free volume was obtained by the Atom Volumes and Surfaces module in MS software according to Connolly surface. Figure 12(a) shows the Connolly surface method to obtain free volume. The atoms of the polymer segment were represented by hard spheres of a van der Waals radius (gray sphere shown in figure 12(a)). The free volume calculated by probe molecule (solvent molecule) (purple sphere in the figure 12(a)) rolling over the Connolly surface and free volume referred to the volume on the side of the Connolly surface without atoms (blue curve in the figure 12(a)). The FFV was defined as free volume/total volume. It should be mentioned that the free volume calculated by the Connolly surface method is not included in the inaccessible volume of the probe.

Therefore, the FFV obtained by a rigid spherical probe was closely related to the size of the probe. As shown in figure 12(b), the FFV of the two membranes decreased while the Connolly radius increased. The FFV of the MWNT/PA-$C_{14}H_{25}O_4$ membrane was larger than that of the PA membrane and the FFV decrease rate with the probe radius increment of the MWNT/PA-$C_{14}H_{25}O_4$ membrane was less than the PA membrane. The first reason was that the average inner diameter after being modified by the long-chain group was 2.8 nm (shown in figure 6), which was much larger than the pore size of the PA membrane and probe radius of the free volume obtained. Another reason was that the empty space of the polymer matrix of the MWNT-$C_{14}H_{25}O_4$/PA membranes was larger than that of the PA, as previous expounded in section 3.3.2. Thus, the molecular surface touched by probe molecules and the FFV of the MWNT/PA-$C_{14}H_{25}O_4$ membrane was greater than that of the PA membrane. Figure 12(c) shows that the free volume of the MWNT-$C_{14}H_{25}O_4$/PA membrane was mainly concentrated at the pore of the MWNT. The fix and larger pore sizes of modified MWNT also explained the increasing FFV of the MWNT-$C_{14}H_{25}O_4$/PA membrane.

As shown in figures 12(d) and (e), pore-size distributions, as indicated in the literature [39], in MWNT-$C_{14}H_{25}O_4$/PA membranes and PA membranes were estimated by the difference value of free volume of adjacent probe radii. The bimodal pore-size distribution of the PA membrane and mono-modal pore-size distribution of the MWNT-$C_{14}H_{25}O_4$/PA membrane were in agreement with the results of Araki *et al* [39] and supported the accuracy of our membrane-building algorithm. As shown in figure 12(d) and table 4, the average pore radius of the PA membrane was 2.41 Å and MWNT-$C_{14}H_{25}O_4$/PA was 3.18 Å, which were near the value of the DRS method. The average pore radius of PA membranes with an MD value of 2.41 Å and DRS value of 2.45 Å were near the experimental pore diameter of 5.1 Å, as reported [53]. This showed the rationality of MD data and DRS data. From the above analyses, the free volume distribution and membranes' pore size supported the conclusion obtained from the DRS data that the pore size of the MWNT-$C_{14}H_{25}O_4$/PA membrane was larger than that of the PA membrane.

3.4.2. Radial distribution function (RDF). RDF is an important characterization method for evaluating the microstructure of materials, which reflects the aggregation characteristics of atoms or molecules. It can be expressed as the probability density of another atom at a distance r around one atom and defined as:

$$g(r) = \frac{dN}{\rho 4\pi r^2 dr}, \tag{11}$$

where ρ is the system density and N is the total number of the system. Figure 13 shows the radial function between polar groups of MWNT-$C_{14}H_{25}O_4$/PA membranes (ester and amide group) and PA membranes (only amide group). The amide bond and ester bond were usually polarized and interact with water by dipole forces such as hydrogen bond shown in the inset chart of figure 13. The increment of the peak intensity of RDF indicated more clustering of water in the MWNT-$C_{14}H_{25}O_4$/PA membrane. These data are in agreement with the conclusion by DRS that water volume fraction f_w and pore dielectric constant ε_p of the MWNT-$C_{14}H_{25}O_4$/PA membrane were greater than that of the PA membrane. This phenomenon could occur because the MWNT/PA-$C_{14}H_{25}O_4$ membrane had better hydrophilicity with the polar oxygen group in the function groups of modified MWNT. It was also verified by

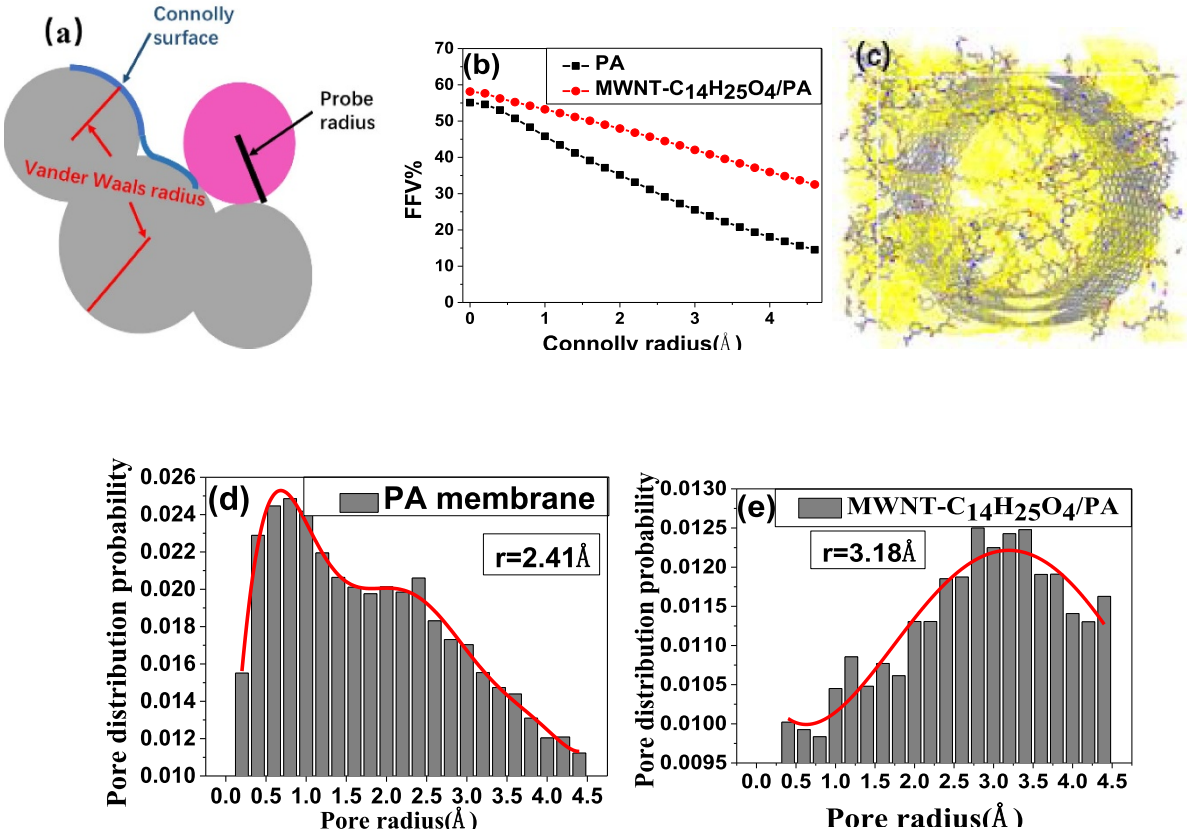

Figure 12. (a) Definition of the Connolly surface, (b) probe radius dependence of FFV of the PA membrane (black line) and MWNT-$C_{14}H_{25}O_4$/PA membrane (red line), (c) simulated morphology of free volume voids (shown in highlight) of the MWNT-$C_{14}H_{25}O_4$/PA membrane model, (d) pore-size distributions of the PA membrane and (e) pore-size distributions of the MWNT/PA-$C_{14}H_{25}O_4$ membrane.

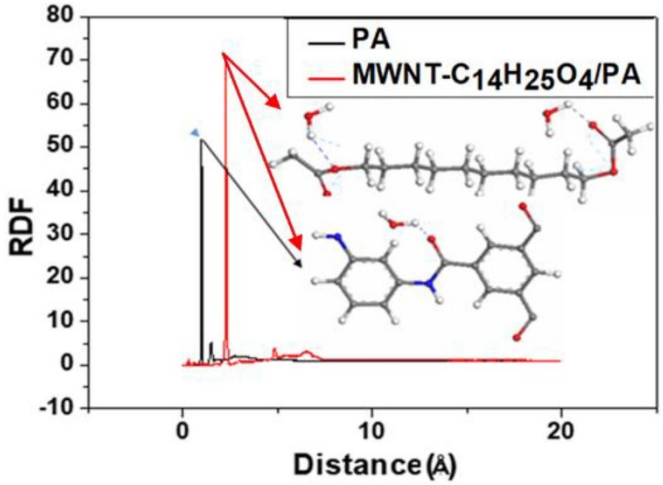

Figure 13. RDFs of water molecules and polar groups of PA (black lines) and MWNT-$C_{14}H_{25}O_4$/PA (red lines) membranes.

experiment data that the MWNT-$C_{14}H_{25}O_4$/PA membrane had a smaller contact angle, as shown in table 1.

3.4.3. Diffusion coefficients. Diffusion coefficients of Na^+, Cl^- and water in membranes were calculated from the slope of their mean square displacements (MSDs) for a long time (1 ns) by Einstein relation (12). The MSDs of water, Na^+ and Cl^- in PA membranes and MWNT-$C_{14}H_{25}O_4$/PA membranes are shown in figure 14.

$$D = \frac{1}{6}\lim_{t\to\infty}\frac{d}{dt}\sum_{i=1}^{Na}\left\langle (r_i(t) - r_i(0))^2\right\rangle, \qquad (12)$$

where D represents diffusion coefficient and $(ri(t) - ri(0))^2$ represents penetrant MSD. The diffusion coefficients of Na^+, Cl^- and water of the MWNT-$C_{14}H_{25}O_4$/PA membranes and PA membrane are listed in table 6. As can be seen in table 6, the diffusion coefficient of water molecules in the MWNT-$C_{14}H_{25}O_4$/PA membranes was larger than that of the PA membrane, while the diffusion coefficients of Na^+ and Cl^- of the MWNT-$C_{14}H_{25}O_4$/PA membranes was smaller than that of the PA membrane. This could occur because ion diffusion was more susceptible to being influenced by factors such as charge and intermolecular force than being only related to the size of free volume. Electrostatic interactions of the PA membrane and MWNT-$C_{14}H_{25}O_4$/PA membrane model calculated by MS software were -2826.16 and -3341.87 KJ mol^{-1}, respectively. And cohesive energy density (CED) of the PA membrane and MWNT/PA-$C_{14}H_{25}O_4$ membrane model were 561.26 and 913.81 J cm^{-3}, respectively (CED can be used to characterize the intermolecular forces of polymer membrane). The larger value of electrostatic force and CED in

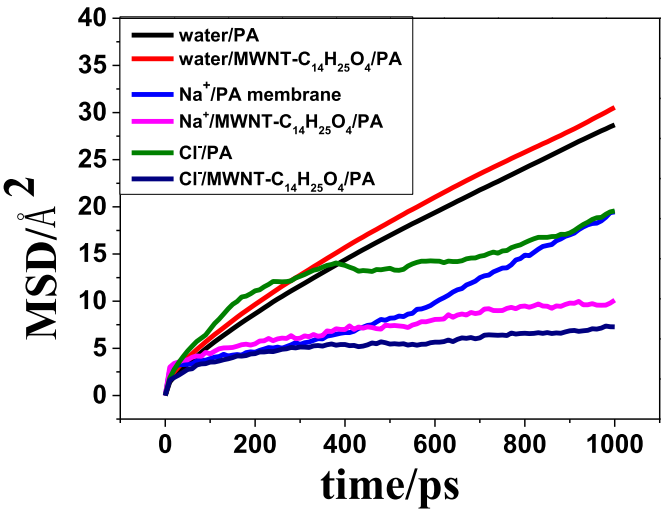

Figure 14. MSD of water, Na^+ and Cl^- in PA membranes and MWNT-$C_{14}H_{25}O_4$/PA membranes.

Table 6. Diffusion coefficients of water, Na^+ and Cl^- in MWNT-C14H25O4/PA membranes and PA membranes.

Membrane	Difusion coefficient (10^{-10} m^2 s^{-1})		
	DH_2O	DNa^+	DCl^-
PA	5.30 ± 0.03	3.35 ± 0.02	2.44 ± 0.02
MWNT-$C_{14}H_{25}O_4$/PA	5.56 ± 0.04	1.33 ± 0.01	0.86 ± 0.01

the MWNT/PA-$C_{14}H_{25}O_4$ membranes indicated that interactions between ions and the MWNT/PA-$C_{14}H_{25}O_4$ membranes were greater than those of the PA membranes. Therefore, although the free volume of the MWNT-$C_{14}H_{25}O_4$/PA membranes was larger than that of the PA membranes, the diffusion rates of Na^+ and Cl^- were smaller than those of the PA membranes. These data showed that the addition of modified MWNT-$C_{14}H_{25}O_4$ could increase the salt rejection of the PA membranes. It was also consistent with the data obtained by the DRS method where the volume charge density and ion solvation energy of the MWNT-$C_{14}H_{25}O_4$/PA were larger than those of the PA membranes.

Therefore, the modified MWNT-$C_{14}H_{25}O_4$ added to the PA membrane might result in high flux and salt rejection by the above analysis of DRS and MD, which suggested a greater potential for desalination than the PA membrane, which is particularly suitable for one-step direct desalination from seawater.

4. Conclusion

In the present study, we copolymerized interior-modification CNT-doped PA membranes, to improve the water permeation and salt rejection of PA membranes. Then the DRS and MD method were used to establish the connection between macroscopic electrical information and microstructure and to characterize the desalination performance of the membranes. The pore dielectric parameters, average pore diameter and water volume fraction of the MWNT-$C_{14}H_{25}O_4$/PA membrane were found to be larger than those of the PA membrane, which exhibited that water flux of the MWNT-$C_{14}H_{25}O_4$/PA membrane was higher than that of the PA membrane. The higher average charge density, ion solvation barrier and reflection coefficient indicate that the adding of interior modified MWNT-$C_{14}H_{25}O_4$ could increase salt rejection of the PA membranes. Using the MD simulation method, PA membrane and 1-ethyl 12-methyl dodecanedioate grafted MWNT/PA membrane models were established and the FFV and diffusion coefficient were calculated by MS software. Results showed that the FFV of the MWNT-$C_{14}H_{25}O_4$/PA membrane and the water diffusion coefficient molecules were larger than those of the PA membranes, while the diffusion coefficients of Na^+ and Cl^- were smaller than those of the PA membranes. These MD results confirmed the results of DRS and the membrane permeation test from the microstructure. Therefore, the combination of DRS and MD provides a fast (short measurement time) and convenient (no pressure device required) method to characterize the water flux and desalination properties of membranes in working condition from theoretical mechanism.

Acknowledgments

This work was financially supported by the National Natural Scientific Foundation of China (Grant Nos. 21173025 and 21473012) and the Major Research Plan of NSFC (Grant No. 21233003).

ORCID iD

Kongshuang Zhao https://orcid.org/0000-0001-5863-2017

References

[1] Mezher T, Fath H, Abbas Z, Khaled A 2011 Techno-economic assessment and environmental impacts of desalination technologies *Desalination* **266** 263–73
[2] Kim C K, Kim J H, Roh I J, Kim J J 2000 The changes of membrane performance with polyamide molecular structure in the reverse osmosis process *J. Memb. Sci.* **165** 189–99
[3] Roh I J, Kim J J and Park S Y 2002 Mechanical properties and reverse osmosis performance of interfacially polymerized polyamide thin films *J. Memb. Sci.* **197** 199–210
[4] Lee K P, Arnot T C and Mattia D 2011 A review of reverse osmosis membrane materials for desalination—development to date and future potential *J. Memb. Sci.* **370** 1–22
[5] Xie W, Geise G M, Freeman B D, Lee H-S, Byun G and McGrath J E 2012 Polyamide interfacial composite membranes prepared from m-phenylene diamine, trimesoyl chloride and a new disulfonated diamine *J. Memb. Sci.* **403–4** 152–61
[6] Jeong B H, Hoek E M V, Yan Y, Subramani A, Huang X, Hurwitz G, Ghosh A K, Jawor A 2007 Interfacial polymerization of thin film nanocomposites: a new concept for reverse osmosis membranes *J. Memb. Sci.* **294** 1–7
[7] Halvorson R A and Vikesland P J 2010 Surface-enhanced Raman spectroscopy (SERS) for environmental analyses *Environ. Sci. Technol.* **44** 7749–55

[8] Drikakis D, Asproulis N and Mantzalis D 2015 Carbon dioxide capture using multi-walled carbon nanotubes *J. Comput. Theor. Nanosci.* **12** 3981–93

[9] Mantzalis D, Asproulis N and Drikakis D 2011 Enhanced carbon dioxide adsorption through carbon nanoscrolls *Phys. Rev.* E **84** 066304

[10] Pushparajalingam J S, Kalweit M, Labois M, Drikakis D 2009 Molecular dynamics of adsorption of argon on graphene, carbon nanotubes and carbon nanotubes bundles *J. Comput. Theor. Nanosci.* **6** 2156–63

[11] Mantzalis D, Asproulis N and Drikakis D 2014 The effects of defects in CO_2 diffusion through carbon nanotubes *Chem. Phys. Lett.* **608** 244–8

[12] Mantzalis D, Asproulis N and Drikakis D 2011 Filtering carbon dioxide through carbon nanotubes *Chem. Phys. Lett.* **506** 81–5

[13] Hummer G, Rasaiah J C and Noworyta J P 2001 Water conduction through the hydrophobic channel of a carbon nanotube *Nature* **414** 188–90

[14] Striolo A 2006 The mechanism of water diffusion in narrow carbon nanotubes *Nano Lett.* **6** 633–9

[15] Holt J K *et al* 2006 Fast mass transport through sub-2-nanometer carbon nanotubes *Science* **312** 1034–7

[16] Majumder M, Chopra N, Andrews R, Hinds B J 2005 Nanoscale hydrodynamics: enhanced flow in carbon nanotubes *Nature* **438** 44

[17] Kim H J, Choi K, Baek Y, Kim D-G, Shim J, Yoon J, Lee J-C 2014 High-performance reverse osmosis CNT/polyamide nanocomposite membrane by controlled interfacial interactions *ACS Appl. Mater. Interfaces* **6** 2819–29

[18] Vatanpour V and Esmaeili M 2014 Fouling reduction and retention increment of polyethersulfone nanofiltration membranes embedded by amine-functionalized multi-walled carbon nanotubes *J. Memb. Sci.* **466** 70–81

[19] Park J, Choi W, Kim S H, Chun B H, Bang J, Lee K B 2010 Enhancement of chlorine resistance in carbon nanotube based nanocomposite reverse osmosis membranes *Desalin. Water Treat.* **15** 198–204

[20] Zhang L, Shi G-Z, Qiu S, Cheng L-H, Chen H-L 2011 Preparation of high-flux thin film nanocomposite reverse osmosis membranes by incorporating functionalized multi-walled carbon nanotubes *Desalin. Water Treat.* **34** 19–24

[21] Zhao H, Qiu S, Wu L, Zhang L, Chen H, Gao C 2014 Improving the performance of polyamide reverse osmosis membrane by incorporation of modified multi-walled carbon nanotubes *J. Memb. Sci.* **450** 249–56

[22] Corry B 2011 Water and ion transport through functionalised carbon nanotubes: implications for desalination technology *Energy Environ. Sci.* **4** 751–9

[23] Chan W F, Chen H-Y, Surapathi A, Taylor M G, Shao X, Marand E, Johnson J K 2013 Zwitterion functionalized carbon nanotube/polyamide nanocomposite membranes for water desalination *ACS Nano* **7** 5308–19

[24] Yang D, Li Q, Shi J, Wang J, Liu Q 2017 Inner surface modification of 1.76 nm diameter (13,13) carbon nanotubes and the desalination behavior of its reverse osmosis membrane *New J. Chem.* **41** 14325–33

[25] Cui Y and Bastien D A 2011 Water transport in human aquaporin-4: molecular dynamics (MD) simulations *Biochem. Biophys. Res. Commun.* **412** 654–9

[26] Tani K, Mitsuma T, Hiroaki Y, Kamegawa A, Nishikawa K, Tanimura Y, Fujiyoshi Y 2009 Mechanism of aquaporin-4's fast and highly selective water conduction and proton exclusion *J. Mol. Biol.* **389** 694–706

[27] Li Q, Yang D, Shi J, Xu X, Yan S, Liu Q 2016 Biomimetic modification of large diameter carbon nanotubes and the desalination behavior of its reverse osmosis membrane *Desalination* **379** 164–71

[28] Li Q *et al* 2018 Modification of (15, 15) 2.034 nm diameter carbon nanotubes with long aliphatic chain and their desalination behavior *Acta Phys. Chim. Sin.* **101** 61–9

[29] Wang J 2018 *Preparation of Modified Carbon Nanotubes Polyamide Membranes with High-Performance* Master's thesis (Qingdao Agricultural University)

[30] Hao W, Yang M, Zhao K, Tang J 2016 Dielectric measurements of fouling of nanofiltration membranes by sparingly soluble salts *J. Memb. Sci.* **497** 339–47

[31] Li Y H and Zhao K S 2004 Dielectric analysis of nanofiltration membrane in electrolyte solutions: influences of electrolyte concentration and species on membrane permeation *J. Colloid Interface Sci.* **276** 68–76

[32] Zhao K and Ni G 2011 Dielectric analysis of nanofiltration membrane in electrolyte solutions: influences of permittivity of wet membrane and volume charge density on ion permeability *J. Electroanal. Chem.* **661** 226–38

[33] Gao Y, Li W, Lay W C L, Coster H G L, Fane A G, Tang C Y 2013 Characterization of forward osmosis membranes by electrochemical impedance spectroscopy *Desalination* **312** 45–51

[34] Efligenir A, Fievet P, Déon S, Salut R 2015 Characterization of the isolated active layer of a NF membrane by electrochemical impedance spectroscopy *J. Memb. Sci.* **477** 172–82

[35] Sim L N, Gu J, Coster H G LFane A G 2016 Quantitative determination of the electrical properties of RO membranes during fouling and cleaning processes using electrical impedance spectroscopy *Desalination* **379** 126–36

[36] Fernandez-Gonzalez C *et al* 2017 Electrochemical impedance spectroscopy of enhanced layered nanocomposite ion exchange membranes *J. Memb. Sci.* **541** 611–20

[37] Wei T, Zhang L, Zhao H, Ma H, Sajib M S J, Jiang H, Murad S 2016 Aromatic polyamide reverse osmosis membrane: an atomistic molecular dynamic simulation *J. Phys. Chem.* B **120** 10311−10318

[38] Ding M, Szymczyk A, Goujon F, Soldera A, Ghoufi A 2014 Structure and dynamics of water confined in a polyamide reverse-osmosis membrane: a molecular-simulation study *J. Memb. Sci.* **458** 236–44

[39] Araki T *et al* 2015 Molecular dynamics study of carbon nanotubes/polyamide reverse osmosis membranes: polymerization, structure, and hydration *ACS Appl. Mater. Interfaces* **7** 24566–75

[40] Araki T, Cruz-Silva R, Tejima S, Ortiz-Medina J, Morelos-Gomez A, Takeuchi K, Hayashi T, Terrones M, Endo M 2018 Water diffusion mechanism in carbon nanotube and polyamide nanocomposite reverse osmosis membranes: a possible percolation-hopping mechanism *Phys. Rev. Appl.* **9** 024018

[41] Asami K *et al* 1973 A method for estimating residual inductance in high frequency AC measurements *Bull. Inst. Chem. Res., Kyoto Univ.* **4** 231–45

[42] Andrea T A, Swope W C and Andersen H C 1983 The role of long ranged forces in determining the structure and properties of liquid water *J. Chem. Phys.* **79** 4576–84

[43] Berendsen H J C, Postma J P M, van Gunsteren W F, DiNola A, Haak J R 1984 Molecular dynamics with coupling to an external bath *J. Chem. Phys.* **81** 3684–90

[44] Sun H 1998 COMPASS: an ab initio force-field optimized for condensed-phase applications overview with details on alkane and benzene compounds *J. Phys. Chem.* B **102** 7338–64

[45] Kuang W and Nelson S O 1997 Low-frequency dielectric dispersion from ion permeability of membranes *J. Colloid Interface Sci.* **193** 242–9

[46] Martinsen Ø G, Grimnes S and Karlsen J 1998 Low frequency dielectric dispersion of microporous membranes in electrolyte solution *J. Colloid Interface Sci.* **199** 107–10

[47] Qing L and Kongshuang Z 2010 Dielectric spectroscopy of a nanofiltration membranes-electrolyte solution system: I. Low-frequency dielectric relaxation from the counterion polarization in pores and model development *J. Phys. Chem.* B **114** 16783–91
[48] Zhang H, Hanai T and KoIzuMt N 1983 Dielectric analysis of interfacial polarization in bilamellar structure as applied to underwater polystyrene films *Bull. Inst. Chem. Res.* **4** 265–81
[49] Zhao K, Asami K and Lei J 2002 Dielectric analysis of chitosan microsphere suspensions: study on its ion adsorption *Colloid Polym. Sci.* **280** 1038–44
[50] Shimazu A, Ikeda K, Miyazaki T, Ito Y 2000 Application of positron annihilation technique to reverse osmosis membrane materials *Radiat. Phys. Chem.* **58** 555–61
[51] Harder E, Walters D E, Bodnar Y D, Faibish R S, Roux B 2009 Molecular dynamics study of a polymeric reverse osmosis membrane *J. Phys. Chem.* B **113** 10177–82
[52] Takashima S 1989 *Electrical Properties of Biopolymers and Membranes* (Philadelphia: Adam Hilger)
[53] Singh P S, Ray P, Xie Z, Hoang M 2012 Synchrotron SAXS to probe cross-linked network of polyamide 'reverse osmosis' and 'nanofiltration' membranes *J. Memb. Sci.* **421–2** 51–9
[54] Senapati S and Chandra A 2001 Dielectric constant of water confined in a nanocavity *J. Phys. Chem.* B **105** 5106–9
[55] Mohammad A W, Hilal N, Al-Zoubi H, Darwish N A 2007 Prediction of permeate fluxes and rejections of highly concentrated salts in nanofiltration membranes *J. Memb. Sci.* **289** 40–50
[56] Vezzani D and Bandini S 2002 Donnan equilibrium and dielectric exclusion for characterization of nanofiltration membranes *Desalination* **149** 477–83
[57] Hagmeyer G and Gimbel R 1998 Modelling the salt rejection of nanofiltration membranes for ternary ion mixtures and for single salts at different pH values *Desalination* **117** 247–56
[58] Bowen W R and Welfoot J S 2002 Modelling the performance of membrane nanofiltration—critical assessment and model development *Chem. Eng. Sci.* **57** 1121–37